Giant energy density via mechanically tailored relaxor ferroelectric behavior of PZT thick film

Mahesh Peddigari, Bo Wang, Rui Wang, Woon-Ha Yoon, Jongmoon Jang, Hyunjong Lee, Kyung Song, Geon-Tae Hwang, Kai Wang, Yuchen Hou, Haribabu Palneedi, Yongke Yan, Han Seung Choi, Jianjun Wang, Aravindkrishna Talluri, Long-Qing Chen, Shashank Priya*, Dae-Yong Jeong*, Jungho Ryu**

M. Peddigari, W.-H. Yoon, J. Jang
Department of Functional Ceramics, Korea Institute of Materials Science (KIMS); Changwon, Gyeongnam 51508, Republic of Korea.

M. Peddigari, A. Talluri
Department of Physics, Indian Institute of Technology Hyderabad, Kandi, Telangana 502284, India.

B. Wang, R. Wang, K. Wang, Y. Hou, H. Palneedi, Y. Yan, J. Wang, L.-Q. Chen, S. Priya
Materials Research Institute/Department of Materials Science and Engineering, Pennsylvania State University; University Park, PA 16802, USA.
E-mail: lqc3@psu.edu, sup103@psu.edu

H. Lee, K. Song
Department of Materials Analysis and Evaluation, Korea Institute of Materials Science (KIMS); Changwon, Gyeongnam 51508, Republic of Korea.

G.-T. Hwang
Department of Materials Science and Engineering, Pukyong National University; Busan 43241, Republic of Korea.

H. S. Choi, J. Ryu
School of Materials Science and Engineering, Yeungnam University; Gyeongsan, Gyeongbuk 38541, Republic of Korea.

D.-Y. Jeong
Department of Materials Science and Engineering, Inha University; Incheon 22212, Republic of Korea.
E-mail: dyjeong@inha.ac.kr

J. Ryu
Institute of Materials Technology, Yeungnam University; Gyeongsan, Gyeongbuk 38541, Republic of Korea.
E-mail: jhryu@ynu.ac.kr

Abstract

Relaxor ferroelectrics (RFEs) are being actively investigated for energy storage applications due to their large electric-field-induced polarization with slim hysteresis and fast energy charging-discharging capability. Here, we report a novel nanograin engineering approach based upon high kinetic energy deposition for mechanically inducing the RFE behavior in a normal ferroelectric $Pb(Zr_{0.52}Ti_{0.48})O_3$ (PZT), which results in simultaneous enhancement in the dielectric breakdown strength (E_{DBS}) and polarization. Mechanically transformed relaxor thick films with 4 μm thickness exhibited an exceptional E_{DBS} of 540 MV/m and reduced hysteresis with large unsaturated polarization (103.6 $\mu C/cm^2$), resulting in a record high energy storage density of 124.1 J/cm^3 and a power density of 64.5 MW/cm^3. This fundamental advancement is correlated with the generalized nanostructure design that comprises of nanocrystalline phases embedded within the amorphous matrix. Microstructure-tailored ferroelectric behavior overcomes the limitations imposed by traditional compositional design methods and provides a feasible pathway for realization of high-performance energy storage materials.

Keywords: energy storage density; breakdown strength; relaxor ferroelectrics; nanograin; amorphous structure; aerosol deposition

1. Introduction

Relaxor ferroelectrics (RFEs) have attracted significant interest for energy storage capacitor applications due to their small polarization (P)–electric field (E) hysteresis, high electric-field-induced polarization, and diffuse phase transition from the ferroelectric (FE) state to the paraelectric (PE) state.[1-3] It is known that these singular characteristics of RFEs originate from polar nanoregions (PNRs), which persist even beyond the FE–PE phase transition as described by Vogel–Fulcher function.[4] As the dimension of nanoscale polar regions in FE materials approaches the critical domain size, the energy barrier for switching can be significantly lowered, thus exhibiting a high dynamic response to external stimuli such as temperature, electric field, and stress.[5] These distinctive features of RFEs are related to the nanoscale structural heterogeneity, so called 'PNRs' resulting from cation order-disorder and the accompanying random electric fields.[6-7] The compositional and charge inhomogeneities associated with the short-range ordering of cations lead to the formation of PNRs/nanodomains within micro-sized grains.[5] In general, the energy storage characteristics of a dielectric capacitor, such as recoverable energy density (U_{rec}) and energy storage efficiency (η), are governed by the electric field-induced polarization (P) and dielectric breakdown strength (E_{DBS}).[8-12] Current knowledge relies on inducing the RFE characteristics for improving the energy storage performance in dielectric ceramics mainly through compositional-heterogeneity driven PNR formation. For example, the composition-modulation-based domain engineering and superparaelectric strategies are widely utilized to scale down the micro-sized domains to highly dynamic PNRs to eliminate the polarization hysteresis and enhance the E_{DBS} in the $BaTiO_3$-based systems.[13-16] Also, the high-entropy approach was adopted to induce the lattice-distorted nano-crystalline grains and disordered amorphous-like phase to improve the E_{DBS} and reduce the polarization switching hysteresis of $Bi_2Ti_2O_7$-based thin films.[17]

Although the U_{rec} achieved using these novel composition-modulating approaches is in the range of 70-182 J/cm^3 and η above 70%, the bottleneck for this superior energy storage performance is at the expense of either polarization or E_{DBS} and the composition- and thickness-specific performance.

Unlike the traditional composition-driven nanodomains/PNRs in ceramics, here we propose a microstructure-driven approach for transforming normal FE system to RFE system by mechanically transforming the microdomains into nanoscale domains. The microstructure comprises of an amorphous matrix with embedded nanocrystalline grains where both the size of the grains and their distribution can be controlled through applied mechanical energy. In soft polymeric FE materials, the similar approach of transforming the uniform microscale structure into PNRs has been first reported by Zhang *et al*., where a normal FE poly(vinylidene fluoride-trifluoroethylene) (P(VDF-TrFE)) copolymer was exposed to high-energy electron irradiation, resulting in the formation of PNRs.[18] Despite the success in the microstructural modification of FE polymers to induce RFE characteristics, achieving similar transformations in FE ceramics remains extremely challenging owing to the strong ionic bonding. Recently, a phase-field simulation-based study demonstrated that vortex, spiral, and in-plane nano polar structures can be stabilized in the strain and thickness-modulated ferroelectric/paraelectric multilayer structures.[19] However, an experimental investigation is yet to be conducted.

In this study, we introduce a novel mechanical energy induced transformation strategy that drives a normal FE thick film such as lead zirconate titanate (Pb(Zr,Ti)O_3; PZT) to exhibit RFE behavior. Our approach transforms the long-range ordered microdomains into highly dense short-range ordered nanograins in the disordered amorphous matrix through a high-kinetic-energy

deposition technique, aerosol deposition (AD). In AD ceramic films, the presence of a highly disordered nonpolar structure around the crystalline nanograins (induced by the high-speed impact of particles on the substrate) significantly enhances the E_{DBS} and delays the electric field dependent polarization/strain saturation.[20-21] The presence of mechanically induced short-range ordered nanograins that are isolated and equidimensional, *i.e.*, nearly identical grain and domain sizes, in the nonpolar matrix leads to formation of flux-closure structure inside the nanograin due to the strong depolarization field caused by the bound charges, which reduces the energy barrier for domain switching.[22] Under these conditions, a higher polarization magnitude under an external field with a slim hysteresis (RFE-like behavior) and enhanced E_{DBS} can be simultaneously achieved in normal FE composition of PZT thick film. The RFE nature is confirmed by modified Curie-Weiss law and Vogel-Fulcher function. These mechanically tailored RFE films with enhanced E_{DBS}, large polarization, and thermal stability have a great potential for replacing the polymer dielectric based capacitors. In addition, the properties of nanograin engineered films can be altered by adjusting the volume fractions and permittivities of the nanograins and amorphous matrix via post-thermal treatments; thus, this approach can be employed to design high-performance materials for specific applications where high breakdown strength, high polarization, and their combination with reduced hysteresis is required.

2. Results and Discussion

2.1. Phase-field modelling

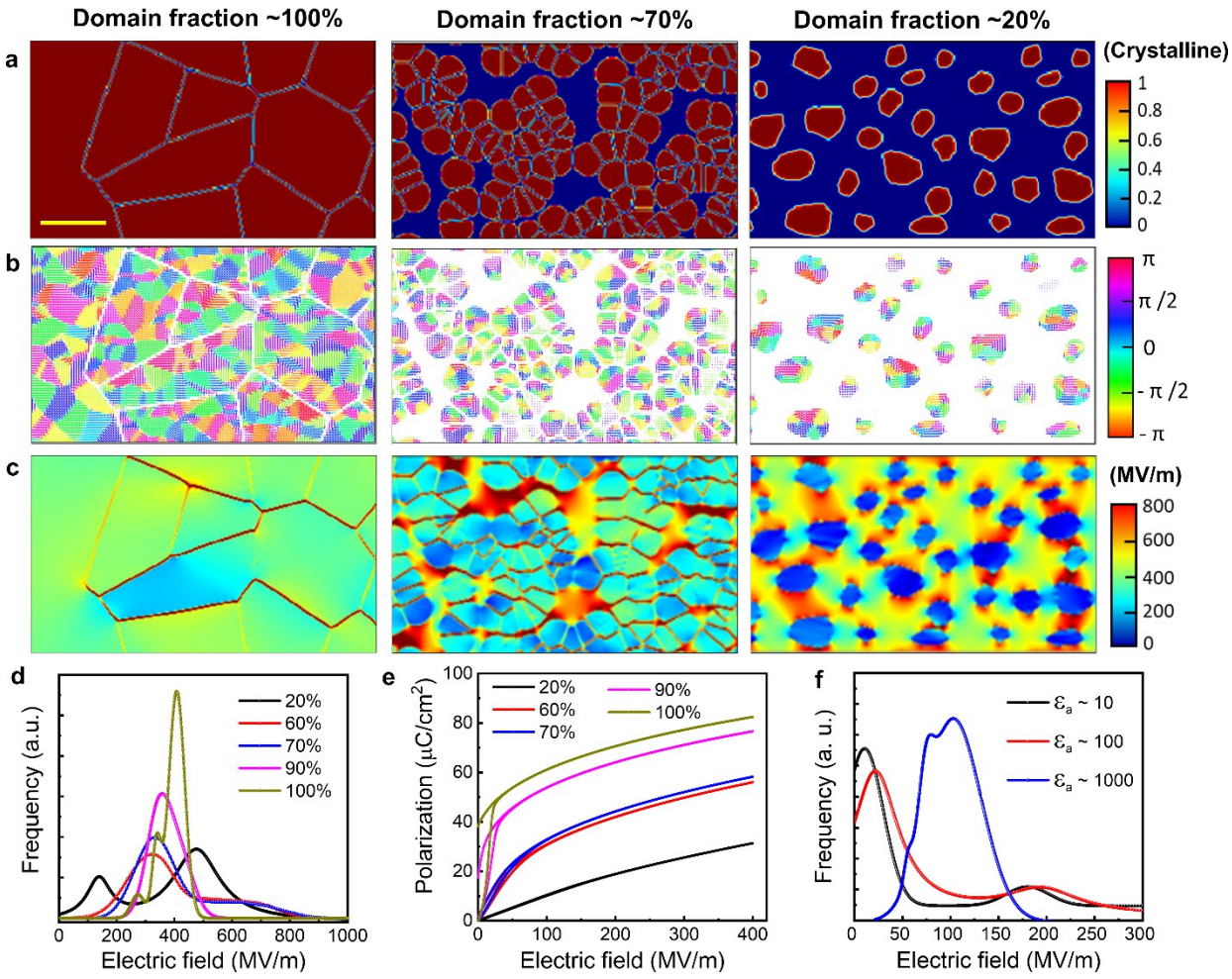

Figure 1. Phase-field modeling of grain and domain structures and microscopic and macroscopic electrical responses of PZT thick films with various volume fractions of nanograins. The simulated (a) grain structures, (b) domain structures of the unpoled state, and (c) electric field distributions of the poled state under an applied electric field of 400 MV/m, respectively, of the PZT films with various volume fractions of the nanograins. (d) The histograms of local electric field magnitude inside the films under an applied electric field of 400 MV/m. (e), Unipolar *P–E* loops with a maximal applied electric field of 400 MV/m. (f) The histograms of local electric field magnitude under an applied electric field of 100 MV/m for PZT films with 60% nanograin volume fraction and various relative permittivity of the amorphous matrix (ε_a). The dimensions of all micrographs are 270 × 160 nm^2 and the yellow scale bar in a is approximately 50 nm.

To demonstrate the equidimensional nanograin engineering concept for inducing the RFE behavior in normal FE composition, we performed phase-field simulations to understand the influence of different nanograin configurations on the electric field endurance limit/distribution

and field-induced polarization hysteresis behavior. We simulated a series of polycrystalline PZT films consisting of randomly oriented nanograins embedded in a nonpolar amorphous matrix (Figure 1a and Figure S1, Supporting Information) with volume fraction of the crystalline phase ranging from 20% to 100%. For each configuration, we obtained corresponding equilibrium domain structures of the unpoled initial films by relaxing the system from a small random noise of polarization at 300 K under zero-electric field (Figure 1b). Then, we slowly applied a unipolar electric field up to E_{max} = 400 MV/m to obtain the spatial (Figure 1c) and statistical distributions (Figure 1d) of the local electric fields under E_{max} as well as the unipolar *P-E* hysteresis loops (Figure 1e). We found that the local electric field magnitude inside the nanograins decreases and the hysteresis of the *P-E* loops reduces when the volume fraction of the nanograins is lower (Figure 1c and Figure S1).[23-25] The higher local electric field tends to concentrate inside the amorphous matrix which can withstand larger electric fields, *i.e.*, has a higher E_{DBS}, and thus may lead to an enhanced electric field endurance limit of the overall film. As a result of the electric field redistribution, the PZT films first show delayed saturation of polarization with reduced remnant polarization (RFE-type behavior) and further show nearly linear dielectric responses with zero remnant polarization (PE-type behavior) as the volume fraction of the nanograins decreases.

The simulation results show that typical dielectric responses of FE-, RFE-, and PE-type are observed for the PZT films with >90%, 60-90%, and <60% nanograin volume fractions, respectively. Although the PE-type exhibits a relatively higher electric field endurance limit and negligible hysteresis due to the presence of a higher fraction of the amorphous phase, the RFE-type displays larger field-induced remnant polarization than the PE-type and a higher electric field endurance limit than the FE-type. Thus, the RFE-type may be the optimal choice for achieving high energy storage density as it enables high applicable electric field (*i.e.*, E_{DBS}) and large electric

field-induced polarization (*i.e*. high dielectric permittivity). It is found that the optimum values of U_{rec} could be achieved with the nanograin volume fractions of 60 to 70 %, while η shows a monotonic decreasing trend due to FE behavior with increase in the nanograin fraction (Figure S2). We found upon further investigation (see Figure 1f and Figure S3) that the relative dielectric permittivity of the nonpolar amorphous matrix (ε_a) also strongly influences the electric field redistribution and the *P-E* hysteresis. When ε_a is as large as the crystalline PZT phase ($\varepsilon_c \sim 1100$), the electric field inside the nanograins increases, leading to the onset of FE behavior. When ε_a is too small, the field redistribution between the nanograins and amorphous phases will limit the maximal applicable electric field, *i.e*., E_{DBS}. Therefore, the key advantage of nanograin engineering with equidimensional grain-domain distribution is that it provides optimum configurations for balancing the FE and PE functionalities as required for energy storage applications without modulating the composition.

2.2. Fabrication of RFE thick films

The fabrication of highly dense nanograined FE ceramics with a conventional high temperature sintering process is a challenging task because of the trade-offs between high density and nanoscale grains. In this context, AD enables the fabrication of highly dense nanograined FE ceramic thick films with a thickness of several microns or more through the fracture of microsized primary particles by the high-kinetic-energy and consolidation of the fractured particles at room temperature.[26-29] Unlike the traditional composition-driven RFEs, the AD process driven mechanical energy induced RFE behaviors will have negligible compositional heterogeneity, which is highly advantageous for operations under high electric fields.

To experimentally demonstrate this approach, we selected a typical normal FE ceramic, undoped $Pb(Zr_{0.52}Ti_{0.48})O_3$, which usually exhibits square hysteretic behavior due to the presence of long-range FE ordering. We successfully fabricated highly dense nanograined PZT thick films with RFE behavior through the AD process. The detailed fabrication process is described in the Experimental section. We deposited PZT thick films with a thickness of 4 μm (Figure S4) to overcome the energy density and operating voltage issues in the bulk and thin film forms.[4] The PZT thick films were annealed at 600 °C for 1 h and 750 °C for 4 h to manipulate the volume fractions and/or relative permittivities of the crystalline nanograins and amorphous matrix. The emphasis here is on the annealed (at 600 °C for 1 h) PZT thick films due to the presence of 60-70% nanosized crystallite fraction within amorphous matrix which results in outstanding energy storage properties.

Figure 2a shows the X-ray diffraction (XRD) patterns of the PZT powder used for the film fabrication and the AD PZT thick films grown on $Pt(111)/Ti/SiO_2/Si(100)$ substrates. Both the PZT powder and the thick films were crystallized in a single perovskite phase. The transmission electron microscopy (TEM) images (Figure 2b and Figure S4) reveal the presence of nano-crystallite domains with a size of 15±5 nm, well dispersed in a highly disordered amorphous matrix having the same composition of nano-crystallites (Figure S5). This heterogeneous microstructure with uniformity in the composition is the result of high-speed collisions between the PZT particles and the substrate during the AD process, which transforms the domain configuration from long-range FE ordering to short-range ordering within a highly disordered nonpolar amorphous matrix. The piezo-response force microscopy (PFM) images revealed that the as-deposited film contains a high degree of disordered structures (indicated in orange) with few randomly oriented nanograins, where the size, density, and polarization of the nanograins were substantially enhanced

after annealing (Figure S6). Despite the enhanced crystallinity, the annealed PZT film still exhibited a continuous distribution of amorphous phase around the crystalline nanograins, as evidenced by the orange color and diffusive FFT patterns in the PFM amplitude (Figure S6) and high-resolution TEM (HRTEM) images (Figure S4), respectively. The obtained microstructure of the annealed AD PZT thick film is in good agreement with our material design strategy (60-70% nanosized crystallite fraction in a nonpolar matrix) and the predictions from the phase-field modeling (Figure 1).

2.3. Behavior of nanograins under the influence of electric field

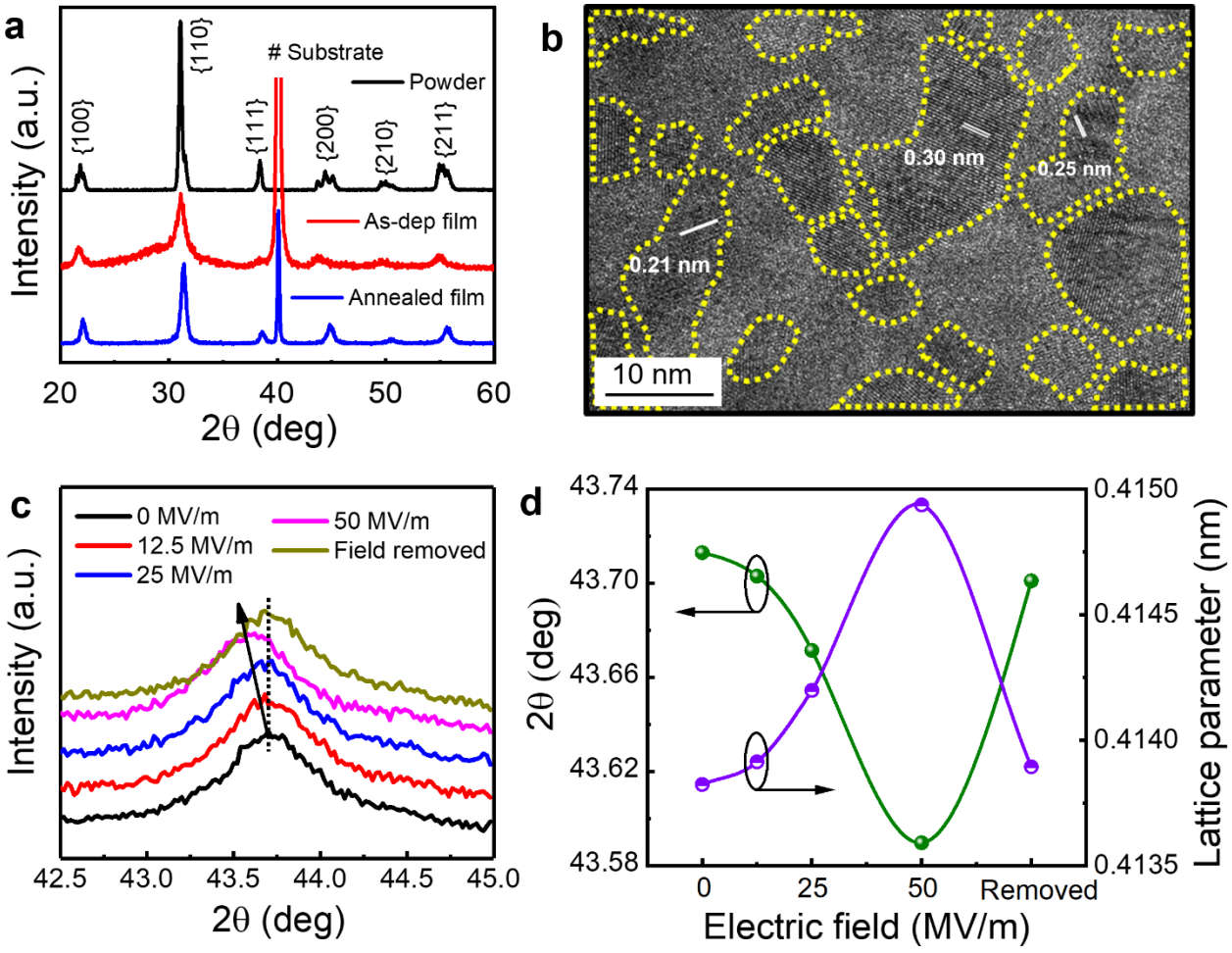

Figure 2. The behaviour of nanograins under the influence of electric field via *in-situ* observation. (a) XRD patterns of the calcined PZT powder, and as-deposited and annealed (at 600 °C for 1 h) films. (b) HRTEM image of PZT thick film, where nanodomains with various interplanar spacings are visible (areas highlighted with yellow dash lines indicate the nanograins). (c and d) *in-situ* XRD measurement showing the out-of-plane structural changes in the nanograin-engineered PZT thick film. (c) XRD patterns of the PZT (200) peak obtained at different electric fields. (d) Variations in the PZT (200) peak position and lattice parameter as a function of the electric field.

We performed *in-situ* XRD and TEM analyses to clarify the crystallographic contributions to the macroscopic polarization properties and switching behavior of the nanograins in the nanograin-engineered PZT thick films (Figure S7). The *in-situ* XRD measurement was performed by collecting the peak profiles of the (200) reflection on the sample surface as a function of the electric field from 0 to 50 MV/m (Figure 2c and 2d). Interestingly, the (200) peak shows a clear shift towards the lower 2θ and an increment of ~ 0.3% in the corresponding lattice parameter with increasing electric field, indicating field-induced domain expansion/lattice elongation along the out-of-plane direction. The diffraction peak returned to its initial position after the removal of the electric field without any considerable changes in the intensity or full width at half maximum, indicating the reversible elongation of the pseudocubic unit cell. Further, the dark-field TEM (DF-TEM) images and corresponding SAED patterns were monitored before and after the electric field application to observe the in-plane structural changes in the PZT thick film (Figure S8). The brightness and size of the nanograins were significantly changed and the lattice parameter was decreased by 0.5% after applying the electric field of 50 MV/m, which is exactly opposite behavior compared to the out-of-plane observation. In addition, the DC-field dependent PFM analysis also supplements the back-switching behavior of nanograins (Figure S9). The effective piezoelectric coefficient (d_{33}^{*}) of the PZT thick film displays a significant AC electric field dependent nonlinear

behavior with a saturated d_{33}^{*} of 157 pm/V (Figure S9), which could be due to the increased nanograins density as evidenced from the field-dependent PFM study.

2.4. Electrical and energy storage properties of nanograin-engineered RFE PZT thick film

The temperature- and frequency-dependent dielectric properties were measured to verify the RFE behavior of the nanograin-engineered PZT thick films (Figure 3a). It is noticed that the PZT thick film exhibited broad and frequency-sensitive dielectric peaks (T_m) with a clear shift in the dielectric peaks towards high temperatures of 314 to 334 °C in the frequency range of 100 Hz to 100 kHz, which is a typical characteristic feature of RFEs. In comparison, the FE PZT bulk ceramic with an average grain size in the micron range as well as the PZT thick films prepared by other conventional techniques exhibited a sharp phase transition at a Curie temperature (T_C) without any frequency dispersion (Figure S10).[30-31] The modified Curie-Weiss law and Vogel-Fulcher equation were adopted to confirm the RFE behavior of nanograin-engineered PZT thick film (Figure S10 and Figure S11). This result demonstrates that the relaxor behavior in FEs can be artificially induced via a mechanical nanograin engineering method beyond any compositional heterogeneity. In addition, the RFE PZT thick film exhibited an outstanding dielectric tunability of 80.4% and an ultralow leakage current density of ~1.7 (33.6) μA/cm^2 at 100 (200) MV/m (Figures. S11-12 and Table S1, Supporting Information).

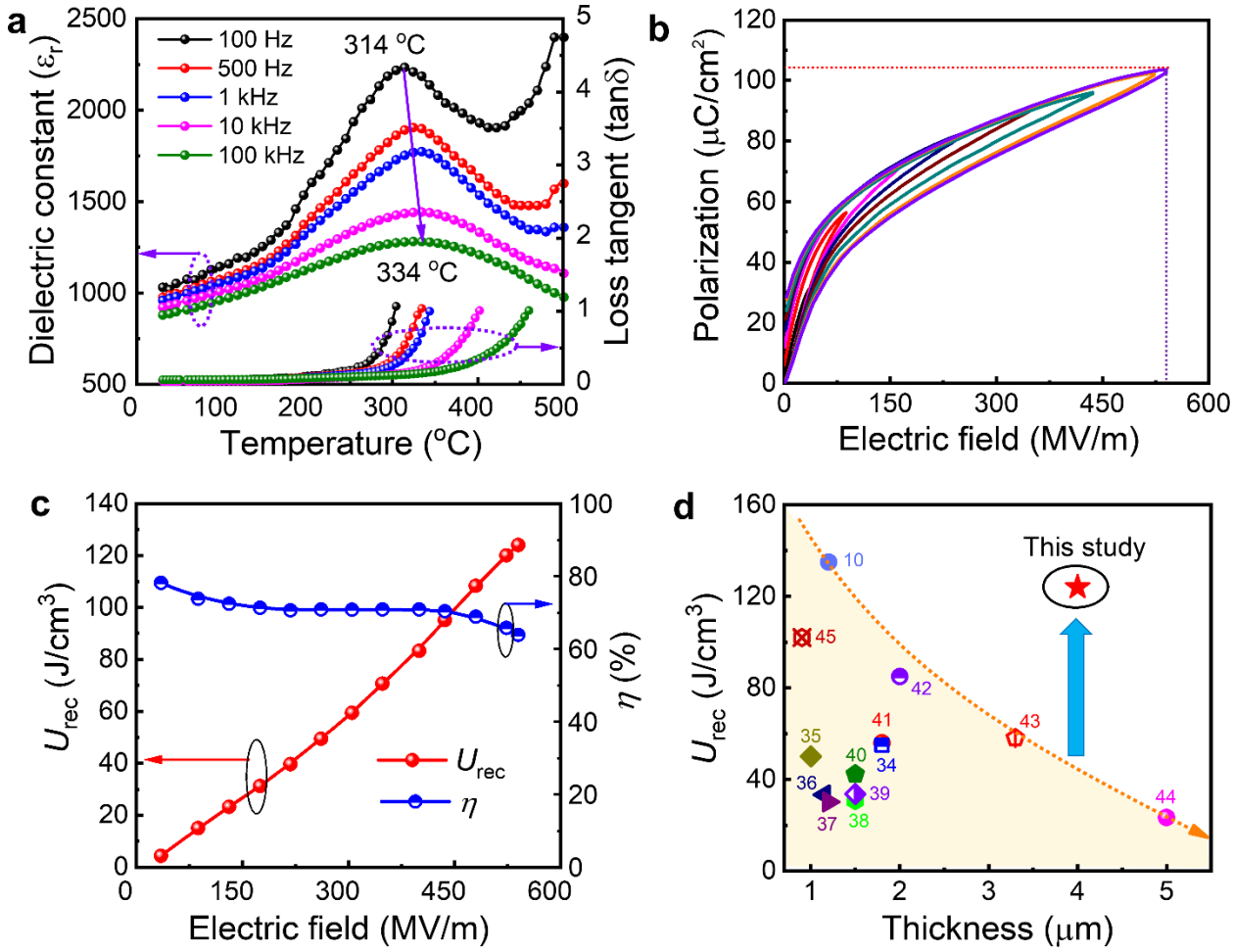

Figure 3. Electrical and energy storage properties of nanograin-engineered PZT thick film. (a) Temperature-dependent dielectric properties (ε_r and $tan\delta$) of the PZT thick film measured at various frequencies (100 Hz to 100 kHz), displaying the diffused phase transition around the Curie temperature with ΔT of 20 °C. (b) Unipolar *P–E* loops of nanograin-engineered PZT thick film measured up to the breakdown field at a frequency of 1 kHz. (c) Recoverable energy density and energy storage efficiency as a function of the electric field estimated using the unipolar *P–E* loops. (d) Comparison of the recoverable energy density of the PZT thick film capacitor with other state-of-the-art dielectric capacitors having a thickness > 0.9 μm.

Because the energy storage capacitors undergo unipolar cycling (charging–discharging) in practice, the unipolar *P–E* hysteresis loops for the RFE PZT thick film were measured until the breakdown occurred. A slim *P–E* hysteresis with a larger ΔP (= $P_m - P_r$) and high E_{DBS} are the critical parameters for achieving high energy storage density and efficiency. Interestingly, the nanograin-engineered RFE PZT thick film sustained ultrahigh electric fields of up to 540 MV/m

(applied voltage of 2160 V), which is equivalent to the typical E_{DBS} of high-performance polymer-based dielectrics[32] and far superior to other ceramic thick films (Figure S13).[10, 13, 22, 33-45] Of particular importance is the observation that despite being thick and polycrystalline form, our PZT films exhibited the same E_{DBS} level as that of thin epitaxial as well as domain-engineered films and outperformed the polycrystalline films with thickness above 0.9 μm. Thus, the nanograin engineered thick films meet the standard of practical applications (Table S2, Supporting Information) requiring a high energy level due to their high voltage (over 1000 V) endurance capacity and easy fabrication route. The nanograin-engineered RFE PZT thick film also exhibited a slim *P–E* hysteresis (ΔP = 75.1 μC/cm^2) with a large as well as unsaturated P_m (103.6 μC/cm^2), as shown in Figure 3b. The comparison of experimental and phase-field modeling data is depicted in Figure S14. We also compared the unipolar *P–E* loops of three different grain-structured films: as-deposited (highly amorphous), nanograin-engineered, and micrograined (high-temperature annealed) PZT thick films of the same composition deposited by AD; the results are depicted in Figure S15. Intriguingly, the PZT thick film with a nanograin-engineered structure exhibited exceptionally higher values of E_{DBS} and polarization compared to that of the other films. The larger E_{DBS} value can be attributed to the enhanced average field strength of the well-dispersed nanograins in the amorphous matrix as predicted from phase field modeling and disappearance of regular meso-scale defects, which are unavoidable in the compositionally driven relaxor ferroelectric ceramics.[45] Such larger values of E_{DBS} and unsaturated P_m with a slim hysteresis loss would greatly enhance the energy storage performance of the PZT thick film. The U_{rec} reached a record-breaking value of 124.1 J/cm^3 with a high η of 64% (Figure 3c) for the thick films owing to the optimized microstructure to simultaneously realize a high E_{DBS} and polarization. The obtained U_{rec} value is many-fold larger than the highly amorphous AD film (35.2 J/cm^3),

micrograined AD film (9.8 J/cm^3), and other dielectric ceramic films (thickness > 1.2 µm) reported by other researchers (Figure 3d).[10, 13, 22, 33-45] In addition, the nanograin-engineered AD PZT thick film showed a negligible variation (within an error range of 5-7%) in the energy storage properties when measured at different frequencies ranging from 10 Hz to 10 kHz (Figure S16). We observed that the nanograin-engineered AD thick films (> 2.5 µm) exhibited a better energy storage performance (reduced E_{DBS}) than thinner films (Figure S17).

2.5. Reliability evaluation and charging-discharging performance

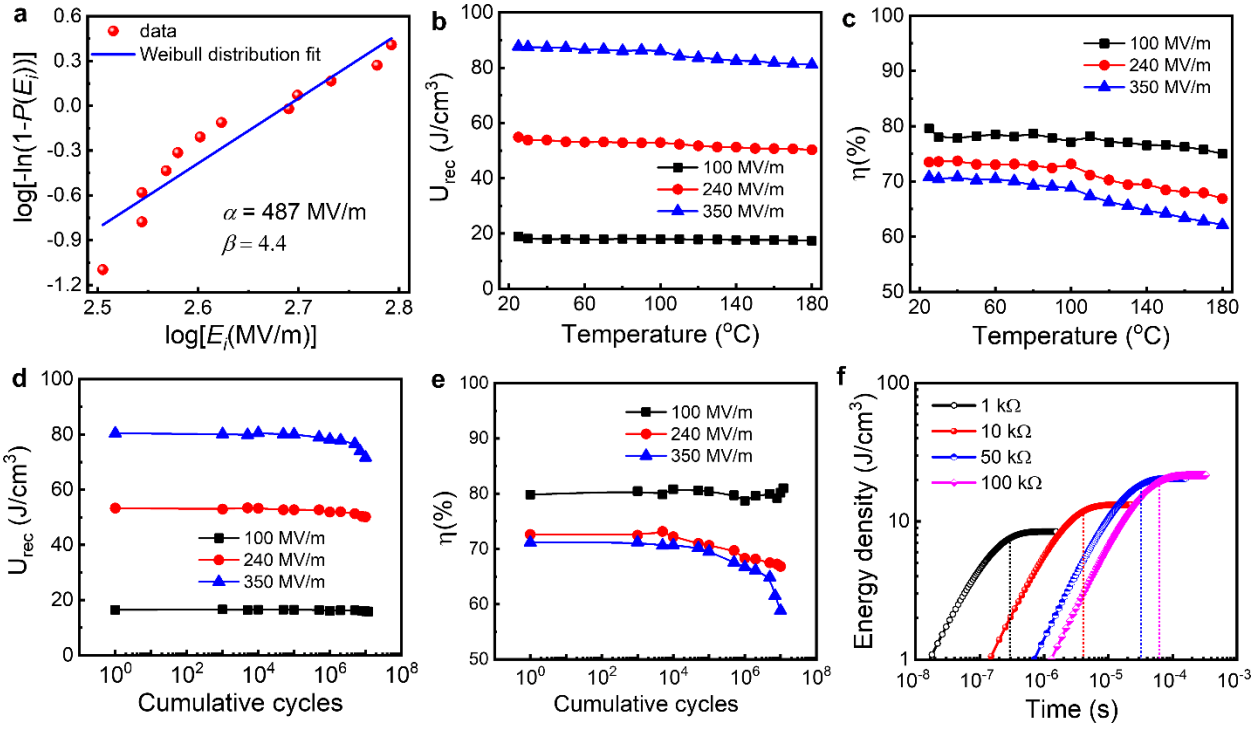

Figure 4. Reliability evaluation and charging–discharging performance of nanograin-engineered RFE PZT thick film. (a) Weibull distribution for estimating the most probable dielectric breakdown field for the PZT thick film. The film displayed (b-c) good thermal stability (20-180 °C) up to E = 350 MV/m and (d-e), excellent fatigue endurance behavior up to E = 240 MV/m. (f) Pulse discharge properties of RFE PZT thick film capacitor. Time-dependent discharged energy density of RFE PZT thick film capacitor measured at 62 MV/m as a function of load resistances.

We analyzed the two-parameter Weibull distribution to estimate the most probable dielectric failure field (α or characteristic E_{DBS}).[4] For this analysis, the statistical values of E_{DBS} were obtained and the distribution was fitted to the Weibull distribution, as shown in Figure 4a. The RFE PZT thick film exhibited an α value of approximately 487 MV/m (applied voltage of 1950 V), which is still higher than that of the ceramic films having a thickness > 1.2 μm (Figure S13). At this characteristic field, the estimated U_{rec} and η are 108.4 J/cm^3 and 70%, respectively (Figure S18). Here, the relatively smaller value of β (~4.4), as compared to the other ceramic thin films with thicknesses below 1 μm, is attributed to the larger ceramic volume. Nonetheless, the practically applicable voltage for our thick films with lowest E_{DBS} is over 1200V.

In order to ensure the reliability of the RFE PZT thick film capacitors, the temperature- and fatigue-cycle-dependent unipolar *P-E* loops were measured at different electric fields from 100 MV/m (~ 400 V) to 350 MV/m (~1400 V). The RFE PZT thick film demonstrated an excellent temperature stability (ΔU_{rec} ~ 7.5% and $\Delta\eta$ ~ 12%) even at 350 MV/m in a broad temperature range of 25-180 ^{o}C (Figures 4b-c and Figure S19). In addition, the RFE PZT thick film showed a better fatigue endurance (ΔU_{rec} < 5.9% and $\Delta\eta$ < 7.9%) up to 240 MV/m and significantly reduced energy storage properties (ΔU_{rec} ~10.9% and $\Delta\eta$ ~17.3%) at 350 MV/m after 10^7 fatigue cycles (Figures 4d-e and Figure S19). Such a high retention of U_{rec} and η even after several charging–discharging electric cycles at larger fields (240 MV/m) may be due to the slim hysteresis and dynamic back-switching behavior of the nanograins under a cyclic electric field.

A high power density (P_d) with a fast discharge time ($\tau_{0.9}$) is another requisite for practical energy storage applications.[32] To evaluate the energy discharge behavior, the RFE PZT thick film capacitor was charged at different electric fields ranging from 25 MV/m (100 V) to 62 MV/m

(250V) and then discharged through the various load resistors (R_L ~ 1-100 kΩ). The values for U_{rec} and P_d were calculated using the voltage decay profile (Figure S20). At an R_L of 1 kΩ, the RFE PZT thick film exhibited a maximum U_{rec} of 8.5 J/cm^3, a superior instantaneous P_d of 64.5 MW/cm^3, and an ultrafast $\tau_{0.9}$ of 290 ns (Figure 4f and Figure S20), which is an excellent match for pulsed power applications. Moreover, the U_{rec} is improved with increasing the R_L while the P_d is decreased due to delayed charge transfer.

These results demonstrate that the fabrication of mechanically tailored RFE ceramic thick films with equidimensional nanograin and domain structures *via* nanograin engineering is an efficient way to achieve ultrahigh energy storage properties. It was confirmed that the AD technique provides highly dense RFE thick films with nanosized grains in highly disordered amorphous matrix. Since this approach relies on the nanograin-architecture composite microstructure design that allows wide range of parameters necessary for high energy density capacitors, it may be applicable to any ferroelectric/dielectric system. Such microstructure realization is beyond the capabilities of traditional composition modification approaches. However, thickness of the film, size of grain and domains, distribution of grain and domains within the 0-3 type composite microstructure, and interface effects need to be co-designed to achieve desired combination of parameters that influence capacitor properties. We believe that these transformative results will have a significant impact on the development of high energy storage density ceramic capacitors.

3. Conclusion

In summary, a mechanical energy induced nanograin engineering approach for transforming normal FEs into RFEs is demonstrated. The RFE behavior in a normal ferroelectric

$Pb(Zr_{0.52}Ti_{0.48})O_3$ (PZT) system is tailored by controlling the size and amount of nanograins in nonpolar matrix. This breakthrough in processing provides nanostructured films which provide a record-breaking energy storage density of 124.1 J/cm^3 under an exceptionally high electric field of 540 MV/m (over 2000 V). As this approach is based on the engineering of nanograins without any compositional modification or complex processing, it holds great promise for inducing the RFE behavior and improving the energy storage performance of dielectrics.

4. Experimental Section

Preparation of PZT powders: Lead zirconate titanate powders of $Pb(Zr_{0.52}Ti_{0.48})O_3$ were prepared using a conventional solid-state reaction method. Stoichiometric amounts of PbO, ZrO_2, and TiO_2 (with a purity > 99.9 %, M/s Sigma-Aldrich) powders were mixed by ball-milling for 24 h in a high-density polyethylene jar with stabilized ZrO_2 balls and anhydrous ethanol as the grinding media. The obtained slurry was dried at 80 °C using a rotary evaporator (N-1300, EYELA) and further calcined at 850 °C for 4 h to induce the single-phase perovskite PZT phase.

Deposition of PZT thick films: Before the deposition, the calcined powders were again ball-milled for 24 h and heat-treated at 500 °C for 2 h to obtain a proper particle size distribution for the AD process. These powders were sieved and mixed with a carrier gas (medical grade dried air) to form an aerosol. A Laval-type nozzle with a rectangular orifice (10 × 0.5 mm^2) was used to feed the particles into the vacuum chamber. The processing parameters such as the particle suspension feed rate (12 L/min), scan speed (1 mm/s), and repetitions (10 cycles) were optimized to obtain a PZT film thickness of 4 μm on a $Pt(111)/Ti/SiO_2/Si(100)$ substrate. Furthermore, the PZT thick films were annealed at 600 °C for 1 h and 750 °C for 4 h (the heating and cooling rates were 1 °C and 0.5 °C, respectively) to improve the density, crystallinity, and grain size. Moreover, PZT pellets

were fabricated using the same powder and sintered at 1220 °C for 2 h to compare the results with the thick films.

Characterization: The phase purity of the PZT powders and thick films was investigated using X-ray diffraction (XRD; D-MAX 2500, Rigaku) with Cu K_α radiation (λ = 0.1506 nm). Scanning electron microscopy (SEM; JSM-5800, JEOL) and transmission electron microscopy (TEM; JEM-2100F, JEOL) were used to observe the microstructure of the thick film. The electric-field-dependent domain response was observed using an *in-situ* TEM system (JEM-2100, JEOL). The electric-field-dependent XRD profiles were obtained using a high-resolution XRD (X'Pert^3 MRD, Malvern Panalytical) equipped with a DC power supply (Keithley, 2290–5) and a homemade fixture. The FE domain structures of the PZT thick films were obtained using piezoelectric response microscopy (PFM, Innova AFM, BRUKER) in the contact mode by varying the DC bias from 0 to 9 V at an AC voltage amplitude of 5 V. Two different shapes of top electrodes, circular (diameters of 0.5 mm & 1 mm) shape for dielectric and ferroelectric measurements (Figure S11a) and rectangular (5mm × 10 mm) shape for in-situ XRD measurement (Figure S7b) were used, and deposited by a DC sputtering system (108, Cressington). The frequency (100 Hz to 100 kHz) and temperature (25–600 °C) -dependent dielectric properties were measured using an RF impedance analyzer (4284, HP) and a high-temperature electric probe system (LABSYS HTEP-8000, Nextron). The temperature-dependent (25–180 °C) FE hysteresis loops were recorded at 1 kHz using a ferroelectric tester (Precision LC-II, Radiant Technologies) by placing the specimen on a hot chuck. The leakage current characteristics were measured using a multimeter (2611A, Keithley). The time-dependent charge–discharge profiles were measured using a homemade high-speed switching circuit and an oscilloscope (WaveSurfer 44Xs-A, LeCroy).

Phase-field simulations: The phase-field simulations were performed to model the formation and evolution of domain structures of the nanograined structures of the PZT thick films under zero-electric field as well as during the unipolar poling process. The simulation procedure includes three steps. First, the phase-field grain-growth model was used to generate a series of nanograined structures with different volume fractions (from 22% to nearly 100%) by controlling the number of initial seeds and the simulation time for grain growth.[46] The multiple grains are treated as the crystalline phase of PZT while the untransformed regions are regarded as the amorphous matrix phase. The grain boundaries are treated as diffuse interfaces whose elastic and electrical properties are linearly interpolated between those of the adjacent grains or amorphous phases. As shown from the experiments, the nanograins of the PZT films exhibit a random distribution of the crystallographic orientation. Therefore, we assigned to each grain *i* a random orientation in terms of three Euler angles, $\theta(i)$, $\phi(i)$, and $\psi(i)$ that follows the Z-X'-Z'' convention. Second, we employed the phase-field model of an inhomogeneous ferroelectric to obtain the polarization distribution at equilibrium in the as-grown unpoled state by quenching the system at 300 K from a small random distribution of polarization.[47] Considering the ~4 μm thickness of the PZT films, the can be, we neglected surface and substrate effects and modelled the system as a stress-free bulk system using three-dimensional periodic boundary conditions. Finally, for each configuration, we applied a unipolar electric field with a one-cycle triangular waveform and a maximal field strength E_{max} up to 400 MV/m to obtain the unipolar *P-E* hysteresis loops. The rate of the applied field is assumed to be slow to obtain the quasi-static responses.

The bulk system is discretized into $420\Delta x \times 160\Delta y \times 1\Delta z$ grid points with real grid spacing $\Delta x = \Delta y = \Delta z = 1$ nm. A dimensionless time step of $\Delta t = 0.01$ is used for evolving the time-dependent Ginzburg-Landau equation for the polarization evolution, i.e., $\frac{\partial \boldsymbol{P}(\boldsymbol{x},t)}{\partial t} = -L\frac{\delta F}{\delta \boldsymbol{P}(\boldsymbol{x},t)}$, where $\boldsymbol{P}(\boldsymbol{x},t)$ is

the spatial-temporal field of the total polarization, L is the kinetic coefficient, and F is the total free energy, which can be obtained by integrating the bulk chemical energy density (f_{bulk}), elastic energy density (f_{elastic}), electrical energy density (f_{electric}), and polarization gradient energy density (f_{grad}) over the system volume V according to the following equation:

$$F = \iiint_v (f_{bulk} + f_{elastic} + f_{electric} + f_{grad}) dV. \quad (4)$$

The detailed expressions of each energy contributions can be found in earlier works.[47] For relaxational simulation under zero electric field, a total timestep of 100,000 was used to obtain the equilibrium polarization configuration. For modeling the unipolar poling process, an applied external electric field is applied along the y axis of the system, which increases linearly from zero to E_{max} in the first 50,000 timesteps and then linearly decreases to zero in another 50,000 timesteps. The detailed formulation and numerical implementations of the phase-field models for grain growth and ferroelectric materials have been documented in earlier works.[46, 48] For bulk systems with periodic boundary conditions, the mechanical and electrostatic energies can be conveniently solved in the reciprocal space using the spectral method,[48] while the local inhomogeneities of the mechanical and dielectric properties associated with the crystalline and amorphous phases can be considered by using the Fourier-spectral iterative perturbation method.[47] The materials parameters were taken from literatures for $PbZr_{1-x}Ti_xO_3$ with the mole fraction of Ti to be x = 0.48.[49] The gradient energy coefficient g_{ij} is assumed to be isotropic with a normalized value of 0.6 which gives a 180-degree domain wall width of 1 – 2 nm.

Supporting Information

Supporting Information is available from the Wiley Online Library or from author

Acknowledgements

M. P. and B.W. contributed equally to this work. This work was supported by National Research Foundation of Korea (grant number NRF-2023R1A2C2005864). H.P. and S.P. acknowledge the financial support through DARPA TE3 program (award number: W911NF1620010). B.W., R.W., and L.-Q.C. acknowledge the support by the National Science Foundation (NSF) through Grant No. DMR-2133373. J.J.W. acknowledges the generous support from the Hamer Foundation through a Hamer Professorship at Penn State. Y.Y. acknowledges the financial support through NSF DMR program (award number: 1936432). Y.H. and K.W. acknowledge the financial support through AFOSR Biophysics program (award number: FA9550-20-1-0157). M.P., W.-H.Y, and J.J acknowledge the financial support provided by a National Research Council of Science & Technology (NST) grant by the Korean government (MSIP) (No. CAP-17-04-KRISS) and the Korea Institute of Materials Science Internal R&D program (No. PNK7560). M.P. and A.T. acknowledge the financial support by the Indian Institute of Technology Hyderabad seed grant project (No. SG/IITH/F298/2022-23/SG-157).

Conflict of Interest

The authors declare no competing interests.

Data Availability Statement

The data that support the findings of this study are available from the corresponding author upon reasonable request.

Received:

Revised:

Published online:

References

[1] P. Zhao, H. Wang, L. Wu, L. Chen, Z. Cai, L. Li, X. Wang, *Adv. Energy. Mater.* **2019**, 9, 1803048.

[2] X. Jian, X. Chen, Q. M. Zhang, *Joule* **2019**, 3, 2296.

[3] J. Kim, S. Saremi, M. Acharya, G. Velarde, E. Parsonnet, P. Donahue, A. Qualls, D. Garcia, L. W. Martin, *Science* **2020**, 369, 81.

[4] H. Palneedi, M. Peddigari, G.-T. Hwang, D.-Y. Jeong, J. Ryu, *Adv. Func. Mater.* **2018**, 28, 1803665.

[5] X. Lv, X.-x. Zhang, J. Wu, *J. Mater. Chem. A* **2020**, 8, 10026.

[6] F. Li, S. Zhang, T. Yang, Z. Xu, N. Zhang, G. Liu, J. Wang, J. Wang, Z. Cheng, Z.-G. Ye, J. Luo, T. R. Shrout, L.-Q. Chen, *Nat. Comm.* **2016**, 7, 13807.

[7] F. Li, S. Zhang, D. Damjanovic, L.-Q. Chen, T. R. Shrout, *Adv. Func. Mater.* **2018**, 28, 1801504.

[8] A. R. Jayakrishnan, J. P. B. Silva, K. Kamakshi, D. Dastan, V. Annapureddy, M. Pereira, K. C. Sekhar, *Progress in Materials Science* **2023**, 132, 101046.

[9] J. Li, Z. Shen, X. Chen, S. Yang, W. Zhou, M. Wang, L. Wang, Q. Kou, Y. Liu, Q. Li, Z. Xu, Y. Chang, S. Zhang, F. Li, *Nat. Mater.* **2020**, 19, 999.

[10] Y. Zhao, J. Ouyang, K. Wang, M. Yuan, Y. Gao, Y. Su, H. Cheng, M. Liu, Q. Yang, W. Pan, *Energy Storage Mater.* **2021**, 39, 81.

[11] M. Acharya, E. Banyas, M. Ramesh, Y. Jiang, A. Fernandez, A. Dasgupta, H. Ling, B. Hanrahan, K. Persson, J. B. Neaton, L. W. Martin, *Adv. Mater.* **2022**, 34, 2105967.

[12] L. Zhao, Q. Liu, J. Gao, S. Zhang, J.-F. Li, *Adv. Mater.* **2017**, 29, 1701824.

[13] H. Pan, J. Ma, J. Ma, Q. Zhang, X. Liu, B. Guan, L. Gu, X. Zhang, Y.-J. Zhang, L. Li, Y. Shen, Y.-H. Lin, C.-W. Nan, *Nat. Comm.* **2018**, 9, 1813.

[14] H. Pan, F. Li, Y. Liu, Q. Zhang, M. Wang, S. Lan, Y. Zheng, J. Ma, L. Gu, Y. Shen, P. Yu, S. Zhang, L.-Q. Chen, Y.-H. Lin, C.-W. Nan, *Science* **2019**, 365, 578.

[15] H. Pan, S. Lan, S. Xu, Q. Zhang, H. Yao, Y. Liu, F. Meng, E.-J. Guo, L. Gu, D. Yi, X. Renshaw Wang, H. Huang, J. L. MacManus-Driscoll, L.-Q. Chen, K.-J. Jin, C.-W. Nan, Y.-H. Lin, *Science* **2021**, 374, 100.

[16] L. Chen, N. Wang, Z. Zhang, H. Yu, J. Wu, S. Deng, H. Liu, H. Qi, J. Chen, *Adv. Mater.* **2022**, 34, 2205787.

[17] B. Yang, Y. Zhang, H. Pan, W. Si, Q. Zhang, Z. Shen, Y. Yu, S. Lan, F. Meng, Y. Liu, H. Huang, J. He, L. Gu, S. Zhang, L.-Q. Chen, J. Zhu, C.-W. Nan, Y.-H. Lin, *Nat. Mater.* **2022**, 21, 1074.

[18] Q. M. Zhang, V. Bharti, X. Zhao, *Science* **1998**, 280, 2101.

[19] Y. Liu, J. Liu, H. Pan, X. Cheng, Z. Hong, B. Xu, L.-Q. Chen, C.-W. Nan, Y.-H. Lin, *Adv. Mater.* **2022**, 34, 2108772.

[20] Z. Cai, X. Wang, W. Hong, B. Luo, Q. Zhao, L. Li, *J. Am. Ceram. Soc.* **2018**, 101, 5487.

[21] J. Exner, T. Nazarenus, D. Hanft, J. Kita, R. Moos, *Adv. Mater.* **2020**, 32, 1908104.

[22] H. Pan, F. Li, Y. Liu, Q. Zhang, M. Wang, S. Lan, Y. Zheng, J. Ma, L. Gu, Y. Shen, P. Yu, S. Zhang, L.-Q. Chen, Y.-H. Lin, C.-W. Nan, *Science* **2019**, 365, 578.

[23] N. Liu, Y. Su, G. J. Weng, *J. Appl. Phys.* **2013**, 113, 204106.

[24] J. Xie, H. Liu, Z. Yao, H. Hao, Y. Xie, Z. Li, M. Cao, S. Zhang, *J. Mater. Chem. C* **2019**, 7, 13632.

[25] C. A. Grabowski, S. P. Fillery, N. M. Westing, C. Chi, J. S. Meth, M. F. Durstock, R. A. Vaia, *ACS Appl. Mater. Inter.* **2013**, 5, 5486.

[26] J. Akedo, J.-H. Park, Y. Kawakami, *Jpn. J. Appl. Phys.* **2018**, 57, 07LA02.

[27] J. Ryu, J.-J. Choi, B.-D. Hahn, D.-S. Park, W.-H. Yoon, K.-H. Kim, *Appl. Phys. Lett.* **2007**, 90, 152901.

[28] G.-T. Hwang, V. Annapureddy, J. H. Han, D. J. Joe, C. Baek, D. Y. Park, D. H. Kim, J. H. Park, C. K. Jeong, K.-I. Park, J.-J. Choi, D. K. Kim, J. Ryu, K. J. Lee, *Adv. Energy. Mater.* **2016**, 6, 1600237.

[29] H. Palneedi, D. Maurya, G.-Y. Kim, V. Annapureddy, M.-S. Noh, C.-Y. Kang, J.-W. Kim, J.-J. Choi, S.-Y. Choi, S.-Y. Chung, S.-J. L. Kang, S. Priya, J. Ryu, *Adv. Mater.* **2017**, 29, 1605688.

[30] J.-R. Cheng, W. Zhu, N. Li, L. E. Cross, *Appl. Phys. Lett.* **2002**, 81, 4805.

[31] K. R. Udayakumar, P. J. Schuele, J. Chen, S. B. Krupanidhi, L. E. Cross, *J. Appl. Phys.* **1995**, 77, 3981.

[32] B. Chu, X. Zhou, K. Ren, B. Neese, M. Lin, Q. Wang, F. Bauer, Q. M. Zhang, *Science* **2006**, 313, 334.

[33] H. Pan, S. Lan, S. Xu, Q. Zhang, H. Yao, Y. Liu, F. Meng, E.-J. Guo, L. Gu, D. Yi, X. R. Wang, H. Huang, J. L. MacManus-Driscoll, L.-Q. Chen, K.-J. Jin, C.-W. Nan, Y.-H. Lin, *Science* **2021**, 374, 100.

[34] H. Cheng, J. Ouyang, Y.-X. Zhang, D. Ascienzo, Y. Li, Y.-Y. Zhao, Y. Ren, *Nat. Comm.* **2017**, 8, 1999.

[35] N. Sun, Y. Li, Q. Zhang, X. Hao, *J. Mater. Chem. C* **2018**, 6, 10693.

[36] J. Wang, Y. Li, N. Sun, Q. Zhang, L. Zhang, X. Hao, X. Chou, *J. Alloy. Compd.* **2017**, 727, 596.

[37] J. Wang, N. Sun, Y. Li, Q. Zhang, X. Hao, X. Chou, *Ceram. Int.* **2017**, 43, 7804.

[38] Y. Liu, X. Hao, S. An, *J. Appl. Phys.* **2013**, 114, 174102.

[39] H. Gao, X. Hao, Q. Zhang, S. An, L. B. Kong, *J. Mater. Sci. Mater. Electron.* **2016**, 27, 10309.

[40] H. Gao, N. Sun, Y. Li, Q. Zhang, X. Hao, L. B. Kong, Q. Wang, *Ceram. Int.* **2016**, 42, 16439.

[41] X. Hao, Y. Wang, L. Zhang, L. Zhang, S. An, *Appl. Phys. Lett.* **2013**, 102, 163903.

[42] B. Ma, Z. Hu, R. E. Koritala, T. H. Lee, S. E. Dorris, U. Balachandran, *J. Mater. Sci. Mater. Electron.* **2015**, 26, 9279.

[43] Y. Wang, X. Hao, J. Yang, J. Xu, D. Zhao, *J. Appl. Phys.* **2012**, 112, 034105.

[44] M. Peddigari, H. Palneedi, G.-T. Hwang, K. W. Lim, G.-Y. Kim, D.-Y. Jeong, J. Ryu, *ACS Appl. Mater. Inter.* **2018**, 10, 20720.

[45] K. Wang, J. Ouyang, M. Wuttig, Y.-Y. Zhao, H. Cheng, Y. Zhang, R. Su, J. Yan, X. Zhong, F. Zeng, *Adv. Energy. Mater.* **2020**, 10, 2001778.

[46] D. Fan, L. Q. Chen, *Acta Mater.* **1997**, 45, 611.

[47] J. J. Wang, X. Q. Ma, Q. Li, J. Britson, L.-Q. Chen, *Acta Mater.* **2013**, 61, 7591.

[48] H.-L. Hu, L.-Q. Chen, *J. Am. Ceram. Soc.* **1998**, 81, 492.

[49] M. J. Haun, Z. Q. Zhuang, E. Furman, S. J. Jang, L. E. Cross, *Ferroelectr.* **1989**, 99, 45.

Table of content

Giant energy density via mechanically tailored relaxor ferroelectric behavior of PZT thick film

Mahesh Peddigari, Bo Wang, Rui Wang, Woon-Ha Yoon, Jongmoon Jang, Hyunjong Lee, Kyung Song, Geon-Tae Hwang, Kai Wang, Yuchen Hou, Haribabu Palneedi, Yongke Yan, Han Seung Choi, Jianjun Wang, Aravindkrishna Talluri, Long-Qing Chen, Shashank Priya*, Dae-Yong Jeong*, Jungho Ryu**

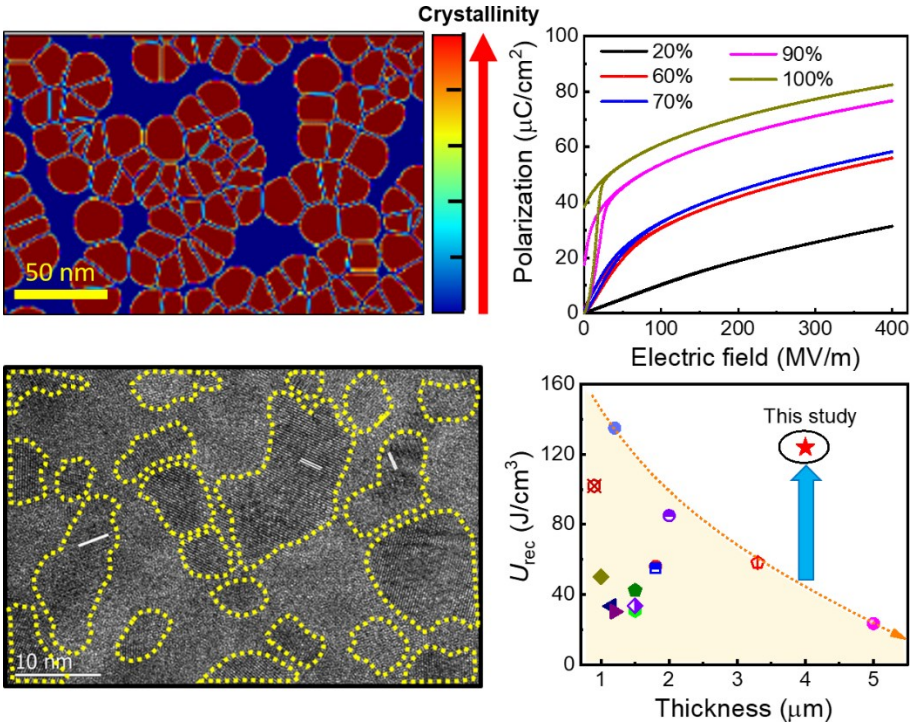

A facile approach, nanograin engineering of normal ferroelectrics beyond compositional modification, to simultaneously enhance the dielectric breakdown strength and polarization with slim hysteresis which is typical behavior of relaxor ferroelectrics (RFE) is designed and revealed for high energy storage devices. The mechanically transformed RFE thick film (~ 4 μm) delivered a record-high energy density of 124 J/cm^3.